SCIENCE CHINA
Physics, Mechanics & Astronomy

•Article•

January 2023 Vol. 66 No. 1: 217011
https://doi.org/10.1007/s11433-022-1992-x

Multiple Dirac points including potential spin-orbit Dirac points in nonsymmorphic $HfGe_{0.92}Te$

Long Chen[1,2†], Liqin Zhou[1,2†], Ying Zhou[1,2†], Chen Liu[3*], Zhongnan Guo[4], Ke Liao[1,2], Shunye Gao[1,2], Wenhui Fan[1,2], Jinfeng Xu[2,3], Yuxuan Guo[2,3], Jia'ou Wang[3*], Tian Qian[1,2,5], Hongming Weng[1,2,5*], and Gang Wang[1,2,5*]

[1] *Beijing National Laboratory for Condensed Matter Physics, Institute of Physics, Chinese Academy of Sciences, Beijing 100190, China;*
[2] *University of Chinese Academy of Sciences, Beijing 100049, China;*
[3] *Beijing Synchrotron Radiation Facility, Institute of High Energy Physics, Chinese Academy of Sciences, Beijing 100049, China;*
[4] *Department of Chemistry, School of Chemistry and Biological Engineering, University of Science and Technology Beijing, Beijing 100083, China;*
[5] *Songshan Lake Materials Laboratory, Dongguan 523808, China*

Received June 27, 2022; accepted September 2, 2022; published online October 26, 2022

The search for new materials with Dirac points has been a fascinating subject of condensed matter physics. Here we first report the growth and band structure of $HfGe_{0.92}Te$ single crystals featuring three different types of Dirac points. $HfGe_{0.92}Te$ crystallizes in a nonsymmorphic tetragonal space group *P*4/*nmm* (No. 129), having a square Ge-atom plane with vacancies of about 8%. Using angle-resolved photoemission spectroscopy (ARPES), the Dirac nodal line composed of conventional Dirac points vulnerable to spin-orbit coupling (SOC) is observed, accompanied by robust Dirac points protected by the nonsymmorphic symmetry against SOC and vacancies. In particular, spin-orbit Dirac points (SDPs) originating from the surface formed under significant SOC could exist based on ARPES and calculations. Quasi-two-dimensional (quasi-2D) characteristics are confirmed by angular-resolved magnetoresistance. $HfGe_{0.92}Te$ bulk crystals can be easily exfoliated to flakes with a thickness of approximately 5 nm for the quasi-2D nature. Thus, $HfGe_{0.92}Te$ provides a good platform to explore exotic topological phases or topological properties with three different types of Dirac points, which is a potential candidate to achieve novel 2D SDPs.

Dirac points, spin-orbit coupling, quasi-2D characteristics

PACS number(s): 61.66.Fn, 71.15.Mb, 71.18.+y

Citation: L. Chen, L. Zhou, Y. Zhou, C. Liu, Z. Guo, K. Liao, S. Gao, W. Fan, J. Xu, Y. Guo, J. Wang, T. Qian, H. Weng, and G. Wang, Multiple Dirac points including potential spin-orbit Dirac points in nonsymmorphic $HfGe_{0.92}Te$, Sci. China-Phys. Mech. Astron. **66**, 217011 (2023), https://doi.org/10.1007/s11433-022-1992-x

1 Introduction

Exotic topological phases have aroused considerable attention, particularly for the potential application of dissipationless and gapless edge states in spintronic devices [1,2]. The discoveries of topological materials, such as two-dimensional (2D) [3,4] or three-dimensional (3D) [5] topological insulators (TIs), Chern insulators [6-8], topological crystalline insulators (TCIs) [9,10], and topological semimetals such as Dirac [11-14] or Weyl semimetals [15-21], remarkably enhance the varieties and functionalities of materials. The special properties are primarily derived from the

*Corresponding authors (Chen Liu, email: cliu@ihep.ac.cn; Jia'ou Wang, email: wangjo@ihep.ac.cn; Hongming Weng, email: hmweng@iphy.ac.cn; Gang Wang, email: gangwang@iphy.ac.cn)
†These authors contributed equally to this work.

Dirac points with linear dispersions near the Fermi level (E_F) [22]. Thus, the search for new materials with Dirac points has been a central topic in condensed matter physics.

For Dirac point materials, Dirac points with massless Dirac fermion play an essential role in exploring quantum relativistic phenomena. However, Dirac points in most 2D materials are vulnerable against spin-orbit coupling (SOC), which would open a global bulk gap at the Dirac points and introduce topologically protected gapless edge states [23-25]. Considering the effect of SOC, 2D Dirac point materials such as graphene will turn into quantum spin Hall insulators [23] or quantum anomalous Hall insulators [26] with preserved or broken time-reversal symmetry. Thus, a new Dirac point robust against SOC, namely, spin-orbit Dirac points (SDPs), has been theoretically proposed to exist in materials with certain nonsymmorphic symmetries [27]. However, achieving 2D SDPs through experiments remains a challenge because of the structural stability, interference of bulk bands, and the location of the Dirac point away from E_F [28,29]. To date, 2D Dirac points were only observed in α-bismuthene experimentally by using micro-angle-resolved photoemission spectroscopy (μ-ARPES) [30]. Therefore, discovering suitable candidate materials with 2D SDPs is necessary to explore their properties and new topological phases.

Featuring square nets with a nonsymmorphic symmetry, WHM-type materials (W = Zr, Hf, La; H = Si, Ge, Sn, Sb; M = O, S, Se, Te) have been found to be a large pool of topological materials with Dirac points and linear dispersions in a large energy range near E_F [31,32]. Most of the WHM-type materials were proven to be novel Dirac nodal line semimetals [33-36], some of which have linear dispersions in a large energy range near E_F without interference from bulk bands [34,35]. Considering SOC, most of the WHM-type materials can be classified into TCIs as a simple stacking of 2D TIs with gapped Dirac points [37]. Rich exotic properties, including large magnetoresistance (MR) [38], electron-hole tunneling [39], large second harmonic generation effect [40], were observed. Long-sought axionic phases [41] were predicted to exist in WHM-type materials and related compounds. For HfGeM (M = S, Se, and Te) monolayers, 2D SDPs could emerge close to E_F [42]. Compared with common Dirac points, which are vulnerable to SOC [43,44], 2D SDPs can be formed under significant SOC of Hf and robust against SOC, which is essential to intrinsically investigate its unique properties, such as the nonlinear Hall effect [45]. By adjusting the local gaps, spin-helical edge states were also predicted in the HfGeTe monolayer [42]. Despite its exotic states, the experimental study on HfGeTe is hindered by single-crystal growth [46].

Here we reported the growth and band structure of $HfGe_{0.92}Te$ single crystals with vacancies on the Ge square net. A Dirac-cone-like band structure with linear dispersions in a large energy range ($\Delta E \sim 0.6$ eV) was observed along $\overline{M}$-$\overline{\Gamma}$-$\overline{M}$, with crossing points near E_F, which would be gapped under SOC. At a high-symmetry point $\overline{X}$, Dirac points at $E - E_F = -0.4$ eV protected by nonsymmorphic symmetry were observed, accompanied by anisotropic electron pockets with the cone point at $E - E_F = -0.2$ eV. For electron pockets, a split was observed along $\overline{X}$-$\overline{M}$, which may indicate the existence of intrinsic SDP robust against SOC based on our calculation. In addition, the typical twofold anisotropic angular-resolved magnetoresistance (AMR) confirms the quasi-two-dimensional (quasi-2D) characteristics of $HfGe_{0.92}Te$ and $HfGe_{0.92}Te$ bulk crystals, which can be easily exfoliated into thin flakes with a thickness approaching 5 nm, showing a potential application in achieving a 2D monolayer. $HfGe_{0.92}Te$ is a good platform to explore exotic topological phases with three different kinds of Dirac points and comprehensively investigate 2D SDPs considering its location ($|E - E_F| < 0.2$ eV) and quasi-2D nature.

2 Materials and method

(1) Single-crystal growth and characterization

Single crystals of $HfGe_{0.92}Te$ were grown by high-temperature solution method using Ge flux. Hafnium powder (Alfa Aesar, 99.5%), germanium powder (Alfa Aesar, 99.999%), and tellurium powder (Alfa Aesar, 99.9%) were mixed using a molar ratio of 2:11:1 in a fritted alumina crucible set (Canfield crucible set) [47] and sealed in a fused-silica ampoule under vacuum. The sealed ampoule was heated to 1423 K, kept for 5 h, and then slowly cooled down to 1273 K at a rate of 2 K/h. After centrifugation at 1273 K, black, shiny, and air-stable plate-like crystals as large as 2 mm × 2 mm × 0.5 mm were obtained. Single-crystal X-ray diffraction (SCXRD) was performed on a four-circle diffractometer (Rigaku XtaLAB Synergy R-DW, HyPix) at 180 K with multilayer mirror graphite-monochromatized Mo K_α radiation (λ = 0.71073 Å) operated at 50 kV and 40 mA. Powder X-ray diffraction data were collected using a PANalytical X'Pert PRO diffractometer (Cu K_α radiation) operated at 40 kV and 40 mA with a graphite monochromator in a reflection mode (2θ = 5°-100°, step size = 0.017°). Indexing and Rietveld refinement were performed using the DICVOL91 and FULLPROF programs [48]. Elemental analysis was conducted using a scanning electron microscope (Hitachi S-4800) equipped with an electron microprobe analyzer for semi-quantitative elemental analysis in energy-dispersive spectroscopy (EDS) mode. AMR was performed on a physical property measurement system (Quantum Design) at 5 K. Contacts for standard four-probe configuration were established by attaching platinum wires using silver paint, resulting in a contact resistance smaller than 5 Ω. Samples for all measurements were cleaved along (00l) (l = integer) from $HfGe_{0.92}Te$ crystals using a razor

blade.

(2) First-principles calculations

We used the crystal structure of HfGeTe to simulate the electronic structure of $HfGe_{0.92}Te$ because Ge vacancies only affect the chemical potential. The first-principles calculations were performed by using the Vienna *ab initio* simulation package [49]. The generalized gradient approximation (GGA) of the Perdew-Burke-Ernzerhof type was selected to describe the exchange-correlation function [50], and the modified Becke-Johnson potential was used to obtain accurate bulk band results [51,52]. We constructed a monolayer and seven-unit-cell slab model to simulate the surface bands of the material and added 15 Å vacuum layers to minimize the interactions among the layers. Brillouin zone (BZ) integration was sampled by 9 × 9 × 5 k-mesh for 3D bulk and 9 × 9 × 1 for the monolayer and seven-unit-cell slab. The cutoff energy was set to 450 eV. The atomic position of the top and bottom unit cells for the seven-unit-cell slab model was optimized. SOC was taken into account self-consistently. The tight-binding model of HfGeTe was constructed using Wannier90 with Hf 5d, Te 5p, and Ge 4p orbitals, which were based on maximally localized Wannier functions [53]. Fermi surface (FS) planes of HfGeTe were calculated by using the WannierTools package [54]. Interlayer binding energies (E_b) of $HfGe_{0.92}Te$ and HfGeTe were calculated using the GGA, vdW-DF, and optB88-vdW correlation functions.

(3) Electronic structure measurement

Synchrotron ARPES and X-ray photoelectron spectroscopy measurements with various photon energies on $HfGe_{0.92}Te$ were performed at beamline 4B9B of the Beijing Synchrotron Radiation Facility. In addition, a helium discharge lump ($h\nu$ = 21.2 eV) was used as a light source during ARPES measurement. The ARPES system was equipped with a Scienta R4000 electron analyzer and base pressure 9.33×10^{-9} Pa. The overall energy and angular resolution were 17 meV and 0.3°, respectively. $HfGe_{0.92}Te$ single crystals were cleaved *in situ* along the (00*l*) (*l* = integer) plane and measured at 7 K.

(4) Atomic force microscopy (AFM)

Thin flakes of $HfGe_{0.92}Te$ crystals were exfoliated using the scotch-tape method [55] and transferred onto a Si/SiO_2 substrate. AFM of thin flakes was performed using an atomic force microscope (Multimode 8.0, Bruker, USA) in a ScanAsyst mode.

3 Results and discussion

Based on the results of SCXRD (Supporting Information Tables S1 and S2), $HfGe_{0.92}Te$ crystallizes in a nonsymmorphic tetragonal space group *P*4/*nmm* (No. 129) with lattice parameters $a = b = 3.8467(3)$ Å, $c = 8.4551(16)$ Å, and $\alpha = \beta = \gamma = 90°$ (Table S1), featuring a square Ge-atom plane sandwiched by two HfTe layers (Figure 1(a)). As a member of the WHM family, it is similar to the well-known "111"-type iron-based superconductor LiFeAs [56] and isostructural to the nodal line Dirac semimetal ZrSiS [38]. Based on the EDS results (Supporting Information Figure S1), the molar ratio is close to Hf:Ge:Te = 1.02:0.87:1, indicating possible vacancies on the Ge site. Refining site occupancies based on SCXRD data (Table S1), about 8% vacancies were observed in the Ge sublattice, and the formula is finally determined to be $HfGe_{0.92}Te$ because of the higher resolution of SCXRD refinement than EDS. Considering the random distribution of Ge vacancies, $HfGe_{0.92}Te$ should have the same symmetries as those of HfGeTe, including one inversion symmetry, a fourfold axis, three mirror symmetries, and nonsymmorphic *n*-glide mirror perpendicular to the *c* axis. Only (00*l*; *l* = integer) diffraction peaks are observed in the X-ray pattern, indicating that the plate surface is perpendicular to the *c* axis (Figure 1(b)).

As shown in Figure 1(c), the *in situ* core-level spectra after cleavage show characteristic peaks of Hf, Ge, and Te atoms, indicating a clean (001) surface of $HfGe_{0.92}Te$ (Figure S2). Both peaks of Te ($3d_{1/2}$ and $3d_{3/2}$) are split, indicating that two chemical environments of Te ions may exist in the terminated layer. This result may indicate the emergence of the Te-Hf terminal after cleavage (Figure 1(a)), which is consistent with the relatively weak coupling between two adjacent HfTe layers similar to the S-Zr terminal in ZrSiS [40]. For the measured FS near E_F, a diamond-shaped FS formed by the Dirac points along the $\bar{\Gamma}$-$\bar{M}$ direction can be observed (Figure 1(d)), which is similar to the diamond-shaped dispersion observed in ZrSiS [34]. In addition, tiny anisotropic electron pockets exist around $\bar{X}$ (Figure 1(e)), which is distinctly different from the calculations of bulk HfGeTe with no pockets at X (Figure 1(f)). Notably, electron pockets at $\bar{X}$ could exist in the monolayer of HfGeTe [42], and Figure 1(g) shows the FS with electron pockets at $\bar{X}$ in the $\bar{\Gamma}$-$\bar{M}$-$\bar{X}$ plane of the HfGeTe monolayer based on our calculation. This result may indicate that the observed anisotropic electron pockets are obtained from the surface of $HfGe_{0.92}Te$, which has been observed previously in HfSiS [57] and ZrSnTe [58].

Figure 2(a) shows the calculated band dispersion along the high-symmetry lines for the HfGeTe bulk crystal. As previously reported in most WHM-type materials [31], HfGeTe exhibits two kinds of Dirac points: Dirac points on Γ-M (blue circles), which form a diamond-shaped Dirac node line, and fourfold degenerated Dirac points (purple circles) at high-symmetry points of BZ such as X and R. Considering the SOC effect, the Dirac node line is gapped, whereas the fourfold degenerated Dirac points protected by the nonsymmorphic glide planes could survive. Compared with the calculated band dispersion of the bulk crystal, the electron bands at $\bar{X}$ for the monolayer and seven-unit-cell-thick slab were lowered by ~1 eV, forming electron pockets centered at

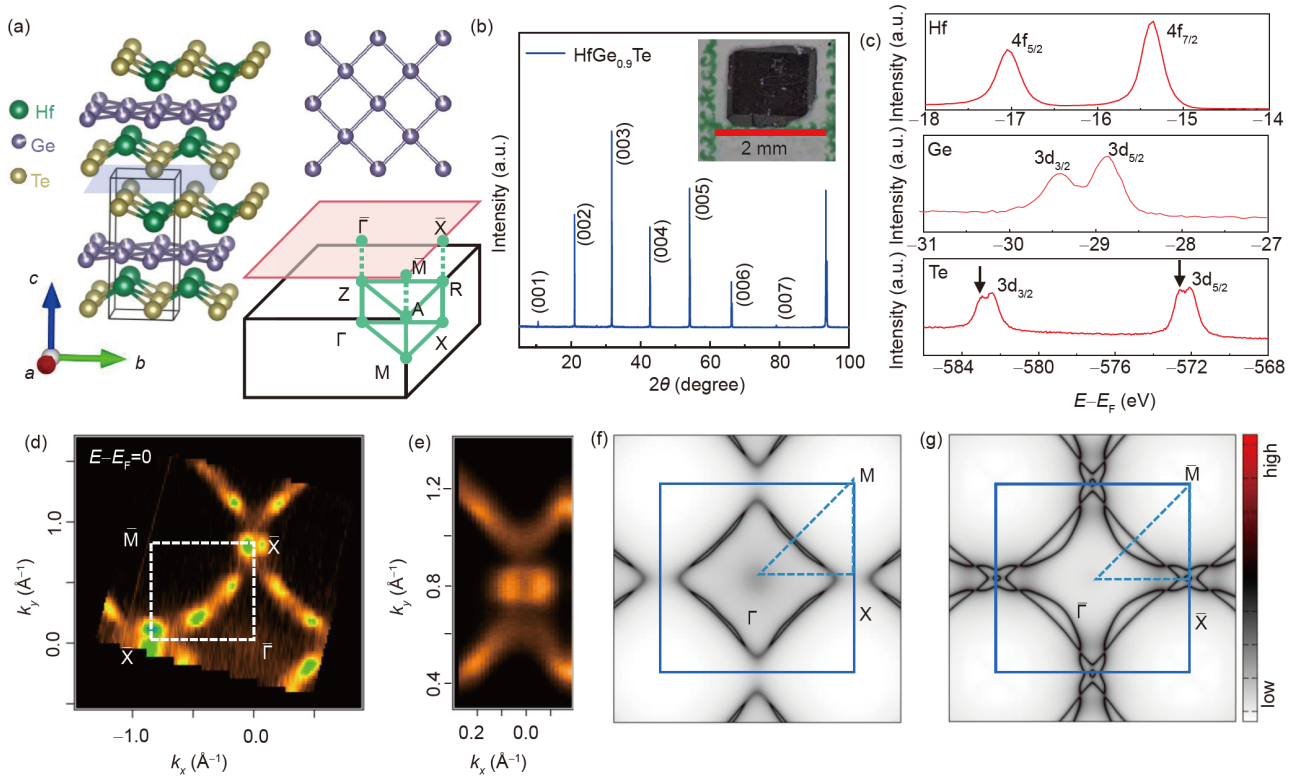

Figure 1 (Color online) Crystal structure and FS of $HfGe_{0.92}Te$. (a) Crystal structure of $HfGe_{0.92}Te$ determined by SCXRD and the BZ of bulk (black) and corresponding surface (red). The light-blue plane indicates the cleavage plane perpendicular to the *c* axis. The black cuboid demonstrates the unit cell and the monolayer used in the calculation. (b) X-ray pattern of $HfGe_{0.92}Te$ single-crystal showing (00*l*; *l* = integer) diffraction peaks. The inset is the optical photograph of a single crystal. (c) Core-level spectra of Hf 4f, Ge 3d, and Te 3d after cleavage. The arrows indicate the split of corresponding peaks. (d) FS intensity plot in the $\overline{\Gamma}$-$\overline{M}$-$\overline{X}$ plane of $HfGe_{0.92}Te$ recorded at $h\nu$ = 46 eV, obtained by integrating the spectral weight within ±10 meV with regard to E_F. (e) Zoomed FS intensity plot around $\overline{X}$. Calculated FS for HfGeTe (f) bulk crystal and (g) monolayer.

$\overline{X}$ (Figure 2(b) and (c)). These pockets are primarily obtained from Hf 5d orbitals, which would lead to an exotic SDP (green circles) when considering the large Rashba SOC effect [42]. For the global gap induced by SOC, the bulk crystal and monolayer of HfGeTe could be classified into a TCI with (Z_2, Z_2, Z_2, Z_4) = (0, 0, 1, 2) [37] and a 2D TI with Z_2 = 1 (Figure S3) [31].

The experimentally observed band structures can be well described using the seven-unit-cell-thick slab of HfGeTe (Figure 2(d)), which is rational considering that the signals of escaped photoelectrons are primarily obtained from several top unit cells close to the terminal in ARPES experiments. Comparing the observed band structures of $HfGe_{0.92}Te$ with the calculated band dispersions of the seven-unit-cell-thick slab of HfGeTe, we found that the only difference is the location of E_F, where the chemical potential shifted by 0.2 eV because of the presence of Ge vacancies. Figure 2(e) shows the band structure along $\overline{M}$-$\overline{\Gamma}$-$\overline{M}$, exhibiting a Dirac-like band structure with crossing points (blue circle) slightly higher than E_F and linear dispersions in a large energy range ($\Delta E \sim 0.6$ eV). As previously described, this kind of Dirac point would be gapped under SOC (Figure 2(a)). The linear dispersions near E_F are hardly affected by vacancy, which may be attributed to the preserved in-plane C_4 symmetry and *n*-glide mirror of the Ge atomic square net. This phenomenon is quite similar to what happened in the monolayer silicene and germylene with hexagonal lattices, where planar and low-buckled materials show similar linear dispersions near the E_F but with slightly different band structures, particularly chemical potential and energy gaps [59]. In the momentum distribution curve (MDC, Figure 2(f)), the feature of multiple bands can be observed and attributed to the parallel bands of the seven-unit-cell-thick slab based on the calculation, which is similar to what happened in ZrSnTe [58].

The band structure of $HfGe_{0.92}Te$ along $\overline{\Gamma}$-$\overline{X}$-$\overline{\Gamma}$ and $\overline{M}$-$\overline{X}$-$\overline{M}$ is summarized in Figure 3. A Dirac-cone-shaped band structure with anisotropic electron pockets around $\overline{X}$ can be clearly observed (Figure 3(c) and (g)), which is consistent with the calculation of the seven-unit-cell-thick slab (Figure 3(d) and (h)). Along $\overline{\Gamma}$-$\overline{X}$-$\overline{\Gamma}$, four sets of dispersions with different intensities can be observed, resulting in different types of Dirac points. The dispersion with the highest intensity (α_2) and the downward linear dispersion (α_3) along $\overline{X}$-$\overline{\Gamma}$ form Dirac points (purple circles) at $\overline{X}$ around $E - E_F$ = −0.4 eV. Based on the calculation and symmetry analysis, the Dirac points at $\overline{X}$ are protected by nonsymmorphic glide

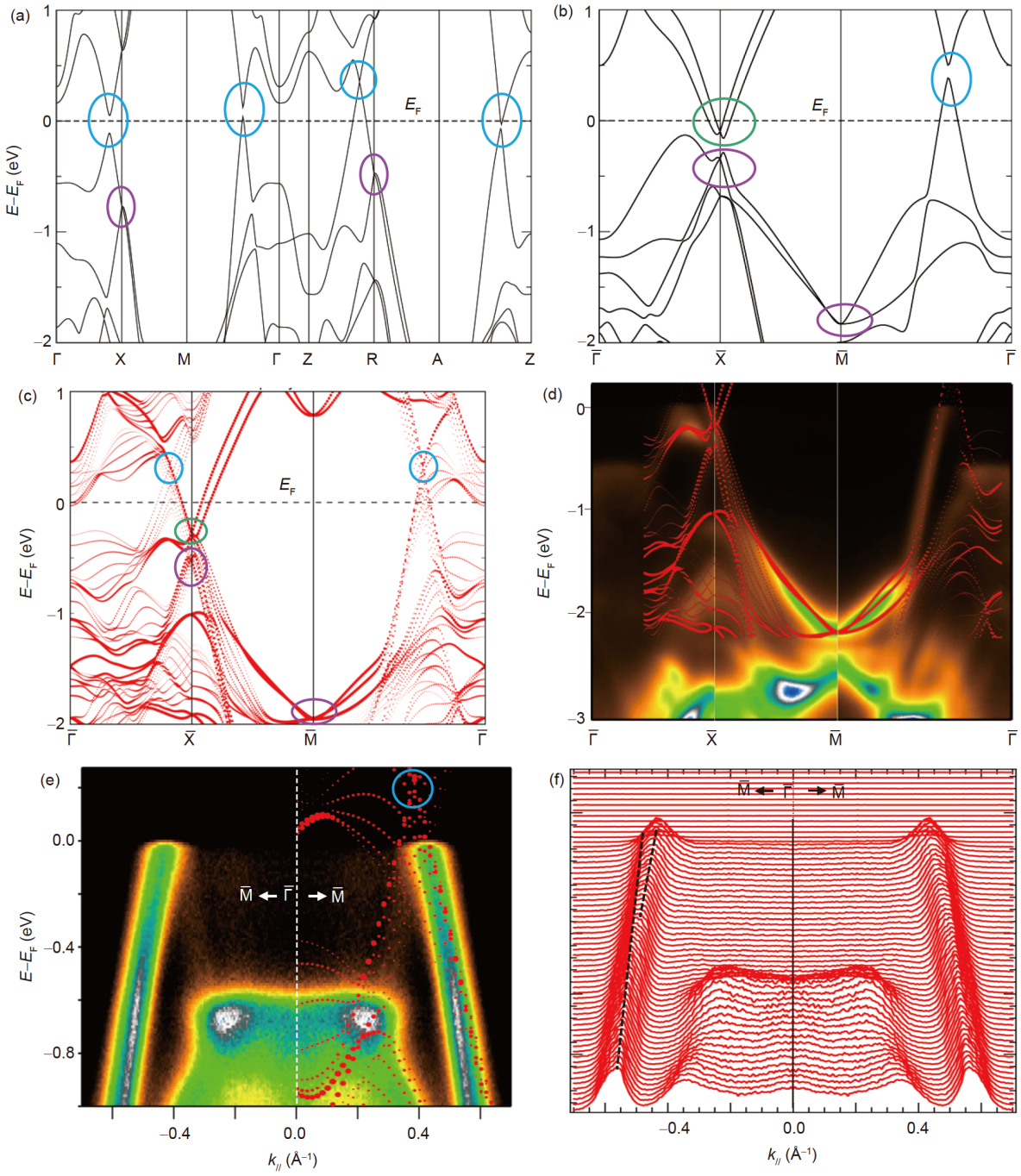

Figure 2 (Color online) Electronic structure of $HfGe_{0.92}Te$. (a)-(c) Calculated band dispersions along the high-symmetry lines with SOC for HfGeTe bulk crystal, monolayer, and a seven-unit-cell-thick slab, respectively. Blue, purple, and green circles highlight three kinds of Dirac points. (d) Experimentally observed band structures for $HfGe_{0.92}Te$ along the high-symmetry lines $\overline{\Gamma}$-$\overline{X}$-$\overline{M}$-$\overline{\Gamma}$ at $h\nu$ = 21 eV. (e) Band structures along $\overline{M}$-$\overline{\Gamma}$-$\overline{M}$ and (f) corresponding MDC. The red dotted lines in (d) and (e) are extracted from the calculation in (c) by lowering E_F to approximately 0.2 eV. The black dotted lines in (f) show multiple band features.

planes and robust against perturbations, particularly the Ge vacancies in the case of $HfGe_{0.92}Te$. The small electron pockets (α_1) crossing E_F with the cone points (green circles) at $E - E_F = -0.2$ eV can be clearly observed, which is different from the calculation of bulk crystals. The linear dispersion with the lowest intensity (α_4) crosses E_F, which would induce the formation of Dirac points above E_F (blue circle in Figure 2(c)). This kind of Dirac points should form Dirac lines combined with the Dirac points along $\overline{M}$-$\overline{X}$-$\overline{M}$ but vulnerable to SOC. Lifting E_F or pumping the electrons above E_F, this kind of Dirac point could be observed. Along $\overline{M}$-$\overline{X}$-$\overline{M}$, the Dirac-cone-shaped band structure should be resolved to the electron pockets with higher intensity (β_1) and the Dirac points with lower intensity (β_2) based on the cal-

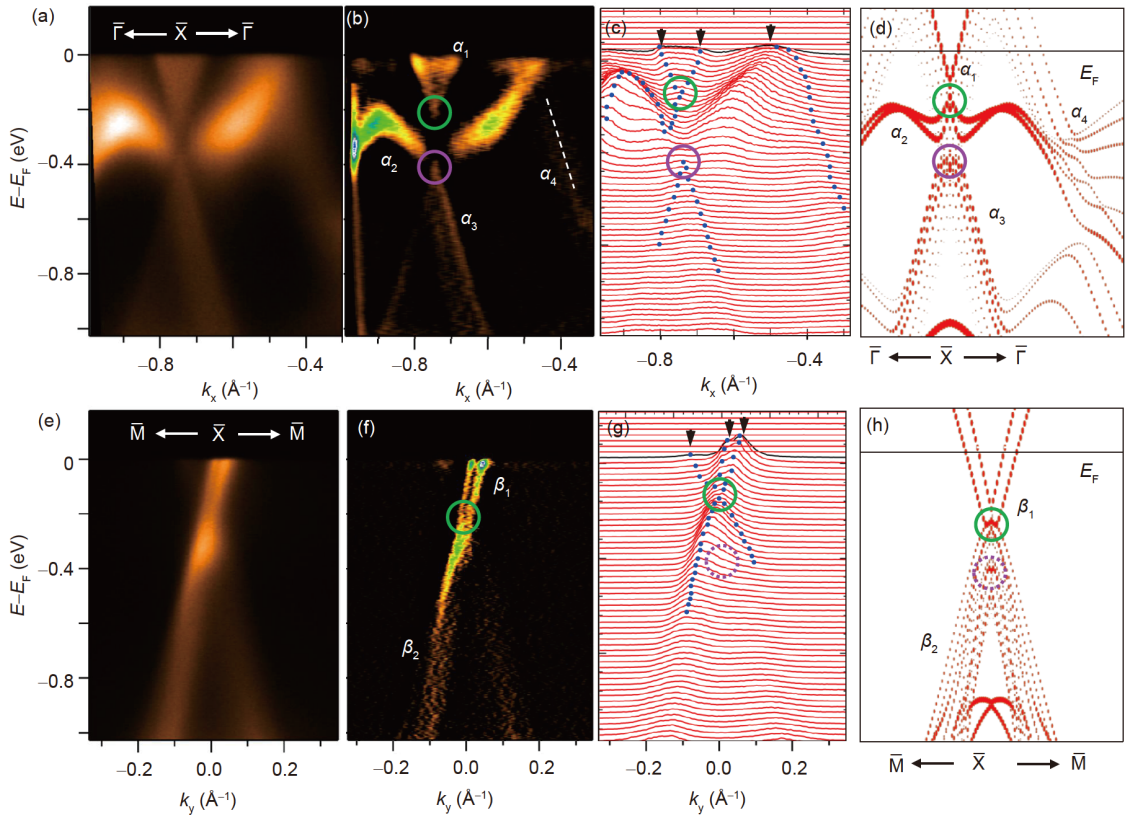

Figure 3 (Color online) Band structure of $HfGe_{0.92}Te$ around $\bar{X}$. (a) Photoemission intensity plot along $\bar{\Gamma}$-$\bar{X}$-$\bar{\Gamma}$ with $h\nu$ = 21.2 eV. (b) Second derivative intensity plot and (c) MDC plot of (a). (d) Calculated band structure along $\bar{\Gamma}$-$\bar{X}$-$\bar{\Gamma}$ for a seven-unit-cell-thick slab. The intensity of the red color indicates the spectral weight projected to the top unit cells. (e)-(h) The same as (a)-(d) but along $\bar{M}$-$\bar{X}$-$\bar{M}$. Purple and green circles highlight two kinds of Dirac points. The arrows indicate the crossings of the dispersion with E_F (black line), and the dotted lines outline the shape of the dispersion.

culation (Figure 3(h)). Given the potential matrix element effect of ARPES measurement, the Dirac points located at $E - E_F = -0.4$ eV are not as clear as that observed along $\bar{\Gamma}$-$\bar{X}$-$\bar{\Gamma}$ (Figure S4).

As shown in the HfGeTe monolayer, a 2D SDP robust against the vacancies and SOC can be formed for the split caused by the Rashba SOC effect of Hf, and the location of the 2D SDP can be tuned by uniaxial strain and biaxial strain or vacancies [42]. For the electron pockets, a clear split was observed in the second derivative intensity and MDC plot (Figure 3(f) and (g)). The split can be regarded as the signal of the existence of SDP in $HfGe_{0.92}Te$, and its location ($E - E_F = -0.2$ eV) is closer to E_F than that of HfSiS ($E - E_F = -0.4$ eV) [57], which has more potential to embed exotic quantum transport properties or applications [42,45]. This SDP is protected by the nonsymmorphic glide plane and time-reversal symmetry of $HfGe_{0.92}Te$, resulting in the degeneracy of the robust against SOC [42]. The split has only been observed in HfSiS [57], not in ZrSiS [34,35] or ZrSnTe [58], which may be attributed to the large SOC effect of Hf with larger atomic mass (Z = 72) than that of Zr (Z = 40).

ARPES intensity maps of the $\bar{\Gamma}$-$\bar{M}$-$\bar{X}$ plane at $E - E_F = -0.3$, -0.4, -0.5, and -0.6 eV were measured with $h\nu$ = 46 eV (Figure 4(a)) to carefully observe the electronic structure of $HfGe_{0.92}Te$ near E_F. Compared with FS of $HfGe_{0.92}Te$, the electron pockets vanish totally at $E - E_F = -0.3$ eV, indicating that the SDP is located quite close to E_F. Further increasing the binding energy from $E - E_F = -0.3$ eV to $E - E_F = -0.6$ eV, a banana-like feature emerges and gradually expands along $\bar{\Gamma}$-$\bar{M}$, which finally evolves into two diamonds at $E - E_F = -0.6$ eV. In addition, small anisotropic hole pockets emerge and expand at $\bar{X}$ (Figure 4(b)), indicating the location of Dirac points protected by nonsymmorphic symmetry. These results were repeatable in the ARPES intensity maps of the $\bar{\Gamma}$-$\bar{M}$-$\bar{X}$ plane measured with $h\nu$ = 21.2 eV (Figure S5).

The band structure along $\bar{X}$-$\bar{R}$ has been measured by varying the photon energy from 20 to 54 eV. As shown in Figure 4(c), only the change in intensity is observed along $\bar{X}$-$\bar{R}$ for $E - E_F > -1$ eV, whereas a clear dispersion exists along $\bar{X}$-$\bar{R}$ for $E - E_F < -1$ eV (Figure S6). This difference indicates the different components of the electronic structure. Given the weak interlayer coupling, the top layer of $HfGe_{0.92}Te$ after cleavage may be reconstructed and may form the SDP at $E - E_F = -0.2$ eV around $\bar{X}$.

Compared with ZrSiS [31,36,60], the reduced interlayer

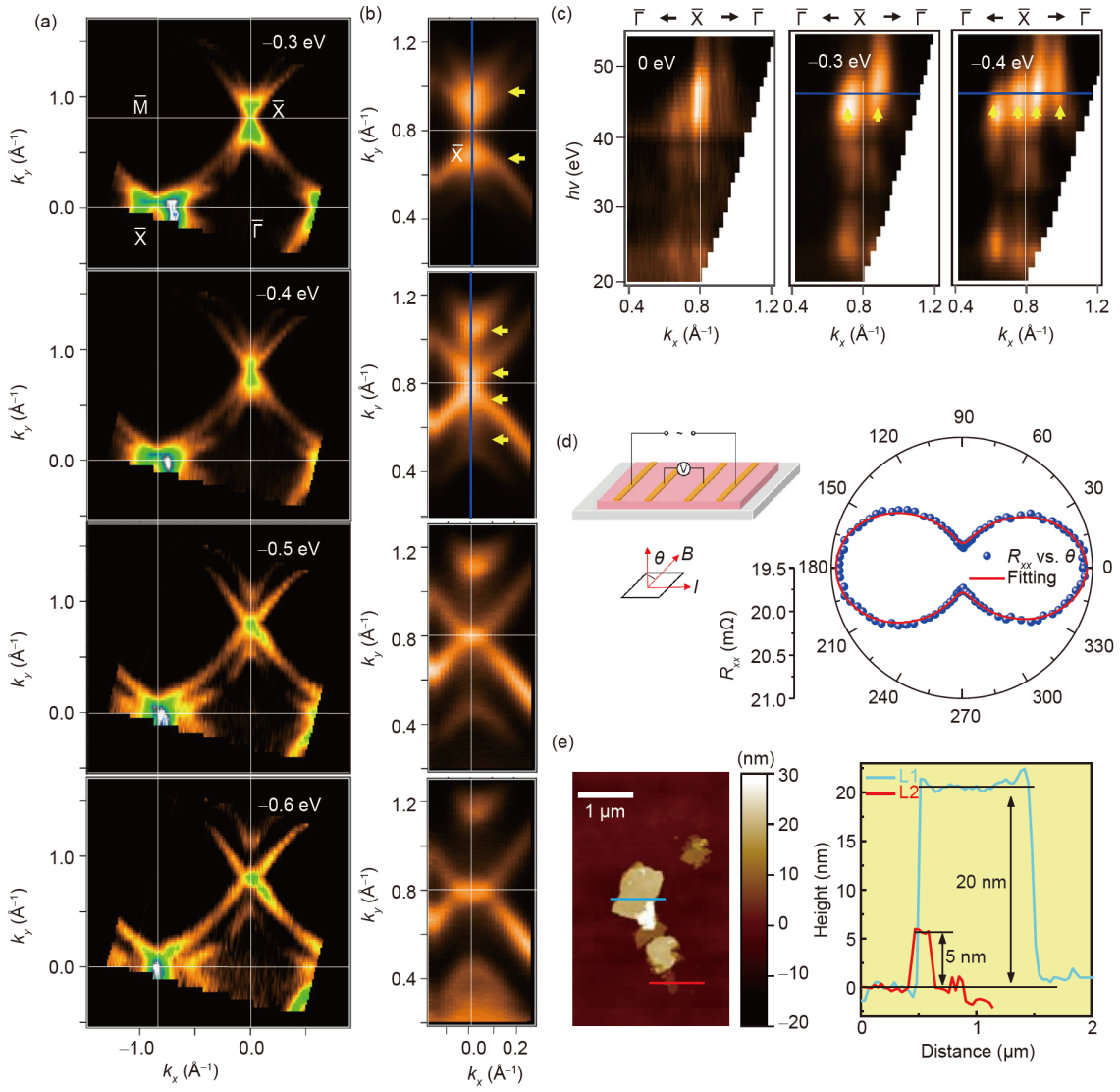

Figure 4 (Color online) 3D band structure and quasi-2D feature of $HfGe_{0.92}Te$. (a) ARPES intensity maps of the $\bar{\Gamma}$-$\bar{M}$-$\bar{X}$ plane at $E - E_F = -0.3$, -0.4, -0.5, and -0.6 eV with $h\nu = 46$ eV. (b) Zoomed ARPES intensity maps of the $\bar{\Gamma}$-$\bar{M}$-$\bar{X}$ plane around $\bar{X}$. (c) Intensity plots of the ARPES data along $\bar{\Gamma}$-$\bar{X}$ at $E - E_F = 0$, -0.3, and -0.4 eV collected in a range of photon energy from 20 to 54 eV. The blue lines and yellow arrows indicate the cut positions and corresponding dispersions in (b) and (c), respectively. (d) Schematic of AMR experimental configuration and polar plot at 9 T for $HfGe_{0.92}Te$. (e) AFM image of thin flakes by exfoliation and corresponding height profile.

coupling further results in some 2D/quasi-2D characteristics of $HfGe_{0.92}Te$ based on AMR and preliminary exfoliation. Applying current in the *ab* plane and the field being rotated in a manner shown in Figure 4(d), the AMR of $HfGe_{0.92}Te$ exhibits a typical twofold anisotropy and classical Lorentz-type MR with AMR $\propto (B\cos\theta)^2$. This behavior can occur in materials with a 2D/quasi-2D feature, such as ZrSiTe [36], whereas a "butterfly-shaped" AMR would be observed in materials with a 3D feature, such as ZrSiS [43,61] or ZrSiSe [36]. Moreover, the 2D/quasi-2D characteristic usually corresponds to a small exfoliation energy or interlayer binding energy [62,63]. In a previous study, the exfoliation energy of the HfGeTe monolayer without vacancy is calculated to be 0.98 J/m^2 [42], which is slightly higher (2-3 times) but at the same magnitude as that of graphene (~0.37 J/m^2) [64] or MoS_2 (~0.41 J/m^2) [65]. Based on the calculated interlayer binding energy of HfGeTe with or without vacancies (Table S3), the interlayer couplings of HfGeTe and $HfGe_{0.92}Te$ are close to each other, showing little effect of vacancies on the interlayer coupling and potential of $HfGe_{0.92}Te$ to reach a monolayer limit by mechanical exfoliation. In our preliminary exfoliation, $HfGe_{0.92}Te$ bulk crystals can be easily exfoliated into thin flakes by using the scotch-tape method. Based on AFM (Figure 4(e)), the thinnest part of the flake is approximately 5 nm (the red line L2), which corresponds to the thickness of about six layers of $HfGe_{0.92}Te$. Optimizing the exfoliation [66], a freestanding $HfGe_{0.92}Te$ monolayer can be obtained in the near future, which provides opportu-

nities to explore the interesting thickness dependence of electronic structures. The quasi-2D nature and SDP near E_F make $HfGe_{0.92}Te$ a good material for device fabrication and a potential candidate to achieve novel 2D SDPs, which has been theoretically predicted in the HfGeTe monolayer [42].

4 Conclusions

We successfully grow single crystals of $HfGe_{0.92}Te$, which belongs to the WHM family but with vacancies on its Ge square net. The experimentally observed band structures of $HfGe_{0.92}Te$ can be well described using the seven-unit-cell-thick slab of HfGeTe, whereas the Ge vacancies only induce hole doping and shifting of chemical potential by 0.2 eV. The Dirac-cone-like band structure with linear dispersions in a large energy range ($\Delta E \sim 0.6$ eV) was observed along $\overline{\Gamma}$-$\overline{\mathrm{M}}$ with its crossing points near E_F, which would be gapped under SOC. At a high-symmetry point $\overline{\mathrm{X}}$, Dirac points protected by nonsymmorphic symmetry and anisotropic electron pockets were observed. For electron pockets, a split was observed along $\overline{\mathrm{X}}$-$\overline{\mathrm{M}}$, which indicates the existence of SDPs under SOC based on our calculation. Thus, three types of Dirac points, namely, the Dirac nodal line with conventional Dirac points vulnerable to SOC, the robust Dirac points protected by the nonsymmorphic symmetry against SOC and vacancies, and potential SDPs derived from the surface, coexist in $HfGe_{0.92}Te$. Typical twofold anisotropic AMR with AMR $\propto (B\cos\theta)^2$ and easy exfoliation show the quasi-2D characteristics of $HfGe_{0.92}Te$, indicating that $HfGe_{0.92}Te$ is a good candidate to explore exotic topological phases or topological properties and is especially promising to realize 2D SDPs considering its quasi-2D nature.

This work was partially supported by the National Natural Science Foundation of China (Grant Nos. 51832010, 51902055, 11925408, 12005251, and 11921004), and National Key Research and Development Program of China (Grant Nos. 2018YFE0202602, 2018YFA0305700, and 2017YFA0302902). L. Chen and G. Wang would like to thank professor X. L. Chen from the Institute of Physics, Chinese Academy of Sciences, for useful discussions.

Supporting Information

The supporting information is available online at http://phys.scichina.com and https://link.springer.com. The supporting materials are published as submitted, without typesetting or editing. The responsibility for scientific accuracy and content remains entirely with the authors.

1 M. Z. Hasan, and C. L. Kane, Rev. Mod. Phys. **82**, 3045 (2010), arXiv: 1002.3895.
2 X. L. Qi, and S. C. Zhang, Rev. Mod. Phys. **83**, 1057 (2011), arXiv: 1008.2026.
3 B. A. Bernevig, T. L. Hughes, and S. C. Zhang, Science **314**, 1757 (2006), arXiv: cond-mat/0611399.
4 M. Konig, S. Wiedmann, C. Brune, A. Roth, H. Buhmann, L. W. Molenkamp, X. L. Qi, and S. C. Zhang, Science **318**, 766 (2007), arXiv: 0710.0582.
5 Y. L. Chen, J. G. Analytis, J. H. Chu, Z. K. Liu, S. K. Mo, X. L. Qi, H. J. Zhang, D. H. Lu, X. Dai, Z. Fang, S. C. Zhang, I. R. Fisher, Z. Hussain, and Z. X. Shen, Science **325**, 178 (2009).
6 R. Yu, W. Zhang, H. J. Zhang, S. C. Zhang, X. Dai, and Z. Fang, Science **329**, 61 (2010), arXiv: 1002.0946.
7 C. Z. Chang, J. Zhang, X. Feng, J. Shen, Z. Zhang, M. Guo, K. Li, Y. Ou, P. Wei, L. L. Wang, Z. Q. Ji, Y. Feng, S. Ji, X. Chen, J. Jia, X. Dai, Z. Fang, S. C. Zhang, K. He, Y. Wang, L. Lu, X. C. Ma, and Q. K. Xue, Science **340**, 167 (2013), arXiv: 1605.08829.
8 H. M. Weng, R. Yu, X. Hu, X. Dai, and Z. Fang, Adv. Phys. **64**, 227 (2015), arXiv: 1508.02967.
9 L. Fu, Phys. Rev. Lett. **106**, 106802 (2011), arXiv: 1010.1802.
10 H. Chen, J. Gao, L. Chen, G. Wang, H. Li, Y. Wang, J. Liu, J. Wang, D. Geng, Q. Zhang, J. Sheng, F. Ye, T. Qian, L. Chen, H. Weng, J. Ma, and X. Chen, Adv. Mater. **34**, 2110664 (2022).
11 Z. Wang, Y. Sun, X. Q. Chen, C. Franchini, G. Xu, H. Weng, X. Dai, and Z. Fang, Phys. Rev. B **85**, 195320 (2012).
12 Z. Wang, H. Weng, Q. Wu, X. Dai, and Z. Fang, Phys. Rev. B **88**, 125427 (2013), arXiv: 1305.6780.
13 Z. K. Liu, B. Zhou, Y. Zhang, Z. J. Wang, H. M. Weng, D. Prabhakaran, S. K. Mo, Z. X. Shen, Z. Fang, X. Dai, Z. Hussain, and Y. L. Chen, Science **343**, 864 (2014), arXiv: 1310.0391.
14 Z. K. Liu, J. Jiang, B. Zhou, Z. J. Wang, Y. Zhang, H. M. Weng, D. Prabhakaran, S. K. Mo, H. Peng, P. Dudin, T. Kim, M. Hoesch, Z. Fang, X. Dai, Z. X. Shen, D. L. Feng, Z. Hussain, and Y. L. Chen, Nat. Mater. **13**, 677 (2014).
15 H. M. Weng, C. Fang, Z. Fang, B. A. Bernevig, and X. Dai, Phys. Rev. X **5**, 011029 (2015), arXiv: 1501.00060.
16 B. Q. Lv, H. M. Weng, B. B. Fu, X. P. Wang, H. Miao, J. Ma, P. Richard, X. C. Huang, L. X. Zhao, G. F. Chen, Z. Fang, X. Dai, T. Qian, and H. Ding, Phys. Rev. X **5**, 031013 (2015), arXiv: 1502.04684.
17 S. M. Huang, S. Y. Xu, I. Belopolski, C. C. Lee, G. Chang, B. K. Wang, N. Alidoust, G. Bian, M. Neupane, C. Zhang, S. Jia, A. Bansil, H. Lin, and M. Z. Hasan, Nat. Commun. **6**, 7373 (2015).
18 S. Y. Xu, I. Belopolski, N. Alidoust, M. Neupane, G. Bian, C. Zhang, R. Sankar, G. Chang, Z. Yuan, C. C. Lee, S. M. Huang, H. Zheng, J. Ma, D. S. Sanchez, B. K. Wang, A. Bansil, F. Chou, P. P. Shibayev, H. Lin, S. Jia, and M. Z. Hasan, Science **349**, 613 (2015), arXiv: 1502.03807.
19 B. Q. Lv, N. Xu, H. M. Weng, J. Z. Ma, P. Richard, X. C. Huang, L. X. Zhao, G. F. Chen, C. E. Matt, F. Bisti, V. N. Strocov, J. Mesot, Z. Fang, X. Dai, T. Qian, M. Shi, and H. Ding, Nat. Phys. **11**, 724 (2015), arXiv: 1503.09188.
20 S. Y. Xu, N. Alidoust, I. Belopolski, Z. Yuan, G. Bian, T. R. Chang, H. Zheng, V. N. Strocov, D. S. Sanchez, G. Chang, C. Zhang, D. Mou, Y. Wu, L. Huang, C. C. Lee, S. M. Huang, B. K. Wang, A. Bansil, H. T. Jeng, T. Neupert, A. Kaminski, H. Lin, S. Jia, and M. Z. Hasan, Nat. Phys. **11**, 748 (2015).
21 C. Liu, J. L. Shen, J. C. Gao, C. J. Yi, D. Liu, T. Xie, L. Yang, S. Danilkin, G. C. Deng, W. H. Wang, S. L. Li, Y. G. Shi, H. M. Weng, E. K. Liu, and H. Q. Luo, Sci. China-Phys. Mech. Astron. **64**, 217062 (2021), arXiv: 2006.07339.
22 E. V. Gorbar, V. A. Miransky, and I. A. Shovkovy, Phys. Rev. B **88**, 165105 (2013), arXiv: 1307.6230.
23 C. L. Kane, and E. J. Mele, Phys. Rev. Lett. **95**, 226801 (2005), arXiv: cond-mat/0411737.
24 H. Q. Huang, Y. Xu, J. F. Wang, and W. H. Duan, WIREs Comput. Mol. Sci. **7**, e1296 (2017).
25 Y. F. Ren, Z. H. Qiao, and Q. Niu, Rep. Prog. Phys. **79**, 066501 (2016), arXiv: 1509.09016.
26 Z. F. Wang, Z. Liu, and F. Liu, Phys. Rev. Lett. **110**, 196801 (2013), arXiv: 1302.1088.
27 S. M. Young, and C. L. Kane, Phys. Rev. Lett. **115**, 126803 (2015), arXiv: 1504.07977.

28 Y. H. Lu, D. Zhou, G. Q. Chang, S. Guan, W. G. Chen, Y. Z. Jiang, J. Z. Jiang, X. S. Wang, S. A. Yang, Y. P. Feng, Y. Kawazoe, and H. Lin, npj Comput. Mater. **2**, 16011 (2016), arXiv: 1509.05629.
29 A. K. Singh, and R. G. Hennig, Appl. Phys. Lett. **105**, 042103 (2014).
30 P. J. Kowalczyk, S. A. Brown, T. Maerkl, Q. Lu, C. K. Chiu, Y. Liu, S. A. Yang, X. Wang, I. Zasada, F. Genuzio, T. O. Menteş, A. Locatelli, T. C. Chiang, and G. Bian, ACS Nano **14**, 1888 (2020).
31 Q. N. Xu, Z. D. Song, S. M. Nie, H. Weng, Z. Fang, and X. Dai, Phys. Rev. B **92**, 205310 (2015), arXiv: 1509.01686.
32 I. Lee, S. I. Hyun, and J. H. Shim, Phys. Rev. B **103**, 165106 (2021).
33 W. Tremel, and R. Hoffmann, J. Am. Chem. Soc. **109**, 124 (1987).
34 L. M. Schoop, M. N. Ali, C. Straßer, A. Topp, A. Varykhalov, D. Marchenko, V. Duppel, S. S. P. Parkin, B. V. Lotsch, and C. R. Ast, Nat. Commun. **7**, 11696 (2016), arXiv: 1509.00861.
35 M. Neupane, I. Belopolski, M. M. Hosen, D. S. Sanchez, R. Sankar, M. Szlawska, S. Y. Xu, K. Dimitri, N. Dhakal, P. Maldonado, P. M. Oppeneer, D. Kaczorowski, F. Chou, M. Z. Hasan, and T. Durakiewicz, Phys. Rev. B **93**, 201104 (2016), arXiv: 1604.00720.
36 J. Hu, Z. J. Tang, J. Y. Liu, X. Liu, Y. L. Zhu, D. Graf, K. Myhro, S. Tran, C. N. Lau, J. Wei, and Z. Q. Mao, Phys. Rev. Lett. **117**, 016602 (2016), arXiv: 1604.06860.
37 T. T. Zhang, Y. Jiang, Z. D. Song, H. Huang, Y. Q. He, Z. Fang, H. M. Weng, and C. Fang, Nature **566**, 475 (2019), arXiv: 1807.08756.
38 Y. Y. Lv, B. B. Zhang, X. Li, S. H. Yao, Y. B. Chen, J. Zhou, S. T. Zhang, M. H. Lu, and Y. F. Chen, Appl. Phys. Lett. **108**, 244101 (2016), arXiv: 1604.01864.
39 M. R. van Delft, S. Pezzini, T. Khouri, C. S. A. Müller, M. Breitkreiz, L. M. Schoop, A. Carrington, N. E. Hussey, and S. Wiedmann, Phys. Rev. Lett. **121**, 256602 (2018), arXiv: 1806.10592.
40 S. M. Chi, F. Liang, H. X. Chen, W. D. Tian, H. Zhang, H. H. Yu, G. Wang, Z. S. Lin, J. P. Hu, and H. J. Zhang, Adv. Mater. **32**, 1904498 (2020).
41 P. Li, B. J. Lv, Y. Fang, W. Guo, Z. Z. Wu, Y. Wu, D. W. Shen, Y. F. Nie, L. Petaccia, C. Cao, Z. A. Xu, and Y. Liu, Sci. China-Phys. Mech. Astron. **64**, 237412 (2021), arXiv: 2011.11267.
42 S. Guan, Y. Liu, Z. M. Yu, S. S. Wang, Y. G. Yao, and S. A. Yang, Phys. Rev. Mater. **1**, 054003 (2017), arXiv: 1706.08692.
43 X. F. Wang, X. C. Pan, M. Gao, J. H. Yu, J. Jiang, J. R. Zhang, H. K. Zuo, M. H. Zhang, Z. X. Wei, W. Niu, Z. C. Xia, X. Wan, Y. L. Chen, F. Q. Song, Y. B. Xu, B. G. Wang, G. H. Wang, and R. Zhang, Adv. Electron. Mater. **2**, 1600228 (2016).
44 Y. Yao, F. Ye, X. L. Qi, S. C. Zhang, and Z. Fang, Phys. Rev. B **75**, 041401 (2007), arXiv: cond-mat/0606350.
45 Y. J. Jin, B. B. Zheng, X. L. Xiao, Z. J. Chen, Y. Xu, and H. Xu, Phys. Rev. Lett. **125**, 116402 (2020), arXiv: 2008.10175.
46 H. Onken, K. Vierheilig, and H. Hahn, Z. Anorg. Allg. Chem. **333**, 267 (1964).
47 P. C. Canfield, T. Kong, U. S. Kaluarachchi, and N. H. Jo, Philos. Mag. **96**, 84 (2016), arXiv: 1509.08131.
48 J. Rodríguez-Carvajal, Phys. B-Condens. Matter **192**, 55 (1993).
49 G. Kresse, and J. Furthmüller, Phys. Rev. B **54**, 11169 (1996).
50 J. P. Perdew, K. Burke, and M. Ernzerhof, Phys. Rev. Lett. **78**, 1396 (1997).
51 F. Tran, and P. Blaha, Phys. Rev. Lett. **102**, 226401 (2009).
52 A. D. Becke, and E. R. Johnson, J. Chem. Phys. **124**, 221101 (2006).
53 A. A. Mostofi, J. R. Yates, G. Pizzi, Y. S. Lee, I. Souza, D. Vanderbilt, and N. Marzari, Comput. Phys. Commun. **185**, 2309 (2014).
54 Q. S. Wu, S. N. Zhang, H. F. Song, M. Troyer, and A. A. Soluyanov, Comput. Phys. Commun. **224**, 405 (2018), arXiv: 1703.07789.
55 R. van Noorden, Nature **483**, S32 (2012).
56 X. C. Wang, Q. Q. Liu, Y. X. Lv, W. B. Gao, L. X. Yang, R. C. Yu, F. Y. Li, and C. Q. Jin, Solid State Commun. **148**, 538 (2008), arXiv: 0806.4688.
57 D. Takane, Z. Wang, S. Souma, K. Nakayama, C. X. Trang, T. Sato, T. Takahashi, and Y. Ando, Phys. Rev. B **94**, 121108 (2016), arXiv: 1606.07957.
58 R. Lou, J. Z. Ma, Q. N. Xu, B. B. Fu, L. Y. Kong, Y. G. Shi, P. Richard, H. M. Weng, Z. Fang, S. S. Sun, Q. Wang, H. C. Lei, T. Qian, H. Ding, and S. C. Wang, Phys. Rev. B **93**, 241104 (2016), arXiv: 1601.07294.
59 C. C. Liu, W. Feng, and Y. Yao, Phys. Rev. Lett. **107**, 076802 (2011), arXiv: 1104.1290.
60 C. C. Wang, and T. Hughbanks, Inorg. Chem. **34**, 5524 (1995).
61 M. N. Ali, L. M. Schoop, C. Garg, J. M. Lippmann, E. Lara, B. Lotsch, and S. S. P. Parkin, Sci. Adv. **2**, e1601742 (2016), arXiv: 1603.09318.
62 W. Wang, S. Y. Dai, X. D. Li, J. R. Yang, D. J. Srolovitz, and Q. S. Zheng, Nat. Commun. **6**, 7853 (2015), arXiv: 1506.00536.
63 J. W. Liu, H. Wang, C. Fang, L. Fu, and X. F. Qian, Nano Lett. **17**, 467 (2017), arXiv: 1605.03903.
64 S. Zhao, Z. Li, and J. Yang, J. Am. Chem. Soc. **136**, 13313 (2014).
65 R. Zacharia, H. Ulbricht, and T. Hertel, Phys. Rev. B **69**, 155406 (2004), arXiv: cond-mat/0308451.
66 M. Yi, and Z. Shen, J. Mater. Chem. A **3**, 11700 (2015).